nature materials

Article

https://doi.org/10.1038/s41563-024-01842-y

Effect of pre-intercalation on Li-ion diffusion mapped by topochemical single-crystal transformation and operando investigation

Received: 26 February 2022

Accepted: 19 February 2024

Published online: 21 March 2024

Check for updates

Yuting Luo[1,2,6], Joseph V. Handy[1,2,6], Tisita Das[3,6], John D. Ponis[1,2,6], Ryan Albers[1,2], Yu-Hsiang Chiang[1,2], Matt Pharr[4], Brian J. Schultz[5], Leonardo Gobbato[5], Dean C. Brown[5], Sudip Chakraborty[3] & Sarbajit Banerjee[1,2]

Limitations in electrochemical performance as well as supply chain challenges have rendered positive electrode materials a critical bottleneck for Li-ion batteries. State-of-the-art Li-ion batteries fall short of accessing theoretical capacities. As such, there is intense interest in the design of strategies that enable the more effective utilization of active intercalation materials. Pre-intercalation with alkali-metal ions has attracted interest as a means of accessing higher reversible capacity and improved rate performance. However, the structural basis for improvements in electrochemical performance remains mostly unexplored. Here we use topochemical single-crystal-to-single-crystal transformations in a tunnel-structured ζ-V_2O_5 positive electrode to illustrate the effect of pre-intercalation in modifying the host lattice and altering diffusion pathways. Furthermore, operando synchrotron X-ray diffraction is used to map Li-ion site preferences and occupancies as a function of the depth of discharge in pre-intercalated materials. Na- and K-ion intercalation 'props open' the one-dimensional tunnel, reduces electrostatic repulsions between inserted Li ions and entirely modifies diffusion pathways, enabling orders of magnitude higher Li-ion diffusivities and accessing higher capacities. Deciphering the atomistic origins of improved performance in pre-intercalated materials on the basis of single-crystal-to-single-crystal topochemical transformation and operando diffraction studies paves the way to site-selective modification approaches for positive electrode design.

Lithium-ion batteries are crucial to the energy transition, from enabling electromobility to addressing the myriad challenges of an entirely reimagined electric grid[1–3]. However, state-of-the-art devices often do not realize the theoretical capacities of insertion electrodes[3,4]. Unlocking the remaining capacity requires the design of materials that adapt to the reversible insertion of Li ions across multiple length scales with minimal distortions[5–7]. Limitations in electrochemical performance as well as supply chain challenges have rendered positive

[1]Department of Chemistry, Texas A&M University, College Station, TX, USA. [2]Department of Materials Science and Engineering, Texas A&M University, College Station, TX, USA. [3]Harish-Chandra Research Institute (HRI) Allahabad, a Constituent Institution of Homi Bhabha National Institute (HBNI), Prayagraj (Allahabad), India. [4]Department of Mechanical Engineering, Texas A&M University, College Station, TX, USA. [5]Dimien Inc., Buffalo, NY, USA. [6]These authors contributed equally: Yuting Luo, Joseph V. Handy, Tisita Das, John D. Ponis. e-mail: sudipchakraborty@hri.res.in; banerjee@chem.tamu.edu

https://doi.org/10.1038/s41563-024-01842-y

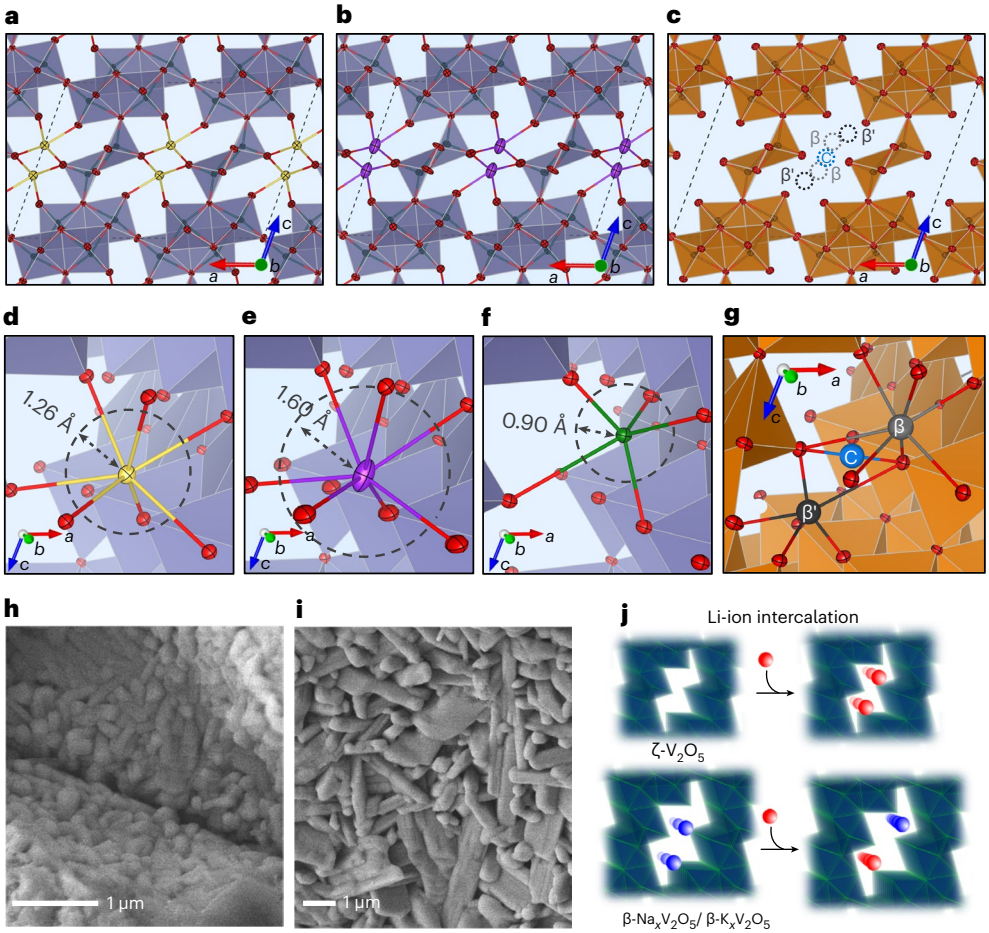

Fig. 1 | Structural and morphological characterization. a,**b**, Refined single-crystal structures of β-$Na_{0.32}V_2O_5$ (**a**) and β-$K_{0.22}V_2O_5$ (**b**) viewed down the *b* axis. Colour key: yellow, Na; purple, K; blue polyhedra, VO_6/VO_5. All thermal ellipsoids shown at 90% probability; unit-cell boundaries indicated by a dashed line. **c**, Single-crystal structure of empty ζ-V_2O_5 viewed down the *b* axis, with vacant β (unit-cell multiplicity 4), β′ (multiplicity 4) and C (multiplicity 2) sites indicated by light-grey, dark-grey and blue dashed circles, respectively. Orange polyhedra, VO_6/VO_5; unit-cell boundaries indicated by a dashed line. **d**–**f**, Perspective views of seven-coordinate β site occupied by Na^+ (**d**) and K^+ (**e**) and five-coordinate β′ site occupied by Li^+ (**f**) within the V_2O_5 tunnel, with dashed lines indicating the Shannon crystal radii of Na (1.26 Å), K (1.60 Å) and Li (0.90 Å). Thermal ellipsoids shown at 60% probability. **g**, Perspective view of the ζ-V_2O_5 tunnel with seven-coordinate β, five-coordinate β′ and two-coordinate C sites indicated by light-grey, dark-grey and blue spheres, respectively. **h**,**i**, Scanning electron microscopy (SEM) images of β-$Na_{0.25}V_2O_5$ (**h**) and β-$K_{0.27}V_2O_5$ (**i**). **j**, Schematic illustration of tunnel expansion induced by Na^+/K^+ chemical pre-intercalation. Refinements of powder XRD patterns of β-$Na_{0.25}V_2O_5$ and β-$K_{0.27}V_2O_5$ are presented in Supplementary Fig. 2.

electrode materials a critical bottleneck[8,9]. An important lever for realizing the full potential of positive electrode materials is the idea of pre-intercalation, wherein (typically) alkali or alkaline-earth cations occupy specific interstitial sites, thereby expanding the galleries between layered materials or propping open three-dimensional (3D) structures[10–12]. In this work, we directly examine the role of alkali-metal-ion pre-intercalation by comparing lithiation/delithiation mechanisms in ζ-V_2O_5, a one-dimensional (1D) tunnel-structured polymorph of V_2O_5, upon pre-intercalation with Na and K ions. By illustrating the dynamical evolution of lithiation-induced structural perturbations using synchrotron-based operando powder X-ray diffraction (XRD) measurements along with high-resolution ex situ single-crystal XRD of topochemical lithiation of macroscopic crystals, and by correlating the observed structure evolution with electrochemical performance, we have deciphered the effect of pre-intercalation on crystal lattice dynamics and diffusion pathways traversed by Li ions.

As a result of its multiple accessible redox couples and limited proclivity for oxygen evolution, V_2O_5 represents an attractive insertion host[13,14]. Moreover, vanadium boasts globally diverse supply chains[15]. Despite appealing economic prospects for vanadium production, lithiation of the thermodynamically stable orthorhombic V_2O_5 triggers distortive and irreversible phase transformations[16]. However, to overcome challenges tied to intercalation-induced structural transformations, V_2O_5 provides a remarkable platform for decoupling composition from structure by exploration of a plethora of metastable polymorphs across its 'rugged' energy landscape[17–19] (Supplementary Fig. 1).

Here, to address the challenges of phase heterogeneity, diffusion limitations and stress gradients[6,19–21], we have identified the 1D tunnel-structured ζ-V_2O_5 polymorph as ideal for accommodating Li ions through a distinctive lithiation mechanism involving cation reordering instead of phase transformations[18,19,22,23]. The ζ-V_2O_5 polymorph alleviates phase heterogeneity, enabling excellent cycling stability and improved rate capability[23]. Chemical pre-intercalation has been used a means of 'pillaring', expanding interlayer spacing in layered structures, to increase accessible capacity and diffusivity[11,24–27]. However, mechanistic understanding of how pre-intercalation affects structure dynamics and diffusion pathways remains unexplored. Here, we grow single crystals of β-$A_xV_2O_5$ (A = Na, K) and topochemically lithiate single crystals, thus providing an atomic-resolution view of pre-intercalation-induced modifications to diffusion pathways. The pre-intercalated materials have further been examined by operando synchrotron powder XRD to examine cation reordering. The pre-intercalation-derived altered

structural dynamics and diffusion pathways are shown to correlate with improved discharge/charge capacities and enhanced Li-ion diffusivities. The results provide mechanistic understanding of the role of pre-intercalation in decreasing the magnitude of lattice modulation and affording alternative diffusion pathways.

Single-crystal structure solutions are shown in Fig. 1a,b for β-$Na_{0.32}V_2O_5$ and β-$K_{0.22}V_2O_5$ (see structural refinement details in Supplementary Tables 1–6), respectively, and are contrasted with the 'empty' metastable 1D polymorph ζ-V_2O_5 (Fig. 1c)[22]. Fig. 1c,g illustrates β, β′ and C interstitial sites available in the tunnels of ζ-V_2O_5[22,28,29]. The pre-intercalated Na and K ions occupy a fraction of interstitial β sites along the tunnels with about 50% occupancy evenly distributed across the β sites[29–31]. Figure 1d,e illustrates the sevenfold distorted pentagonal-bipyramidal local coordination environments of the alkali-metal ions, compared with the fivefold distorted trigonal-bipyramidal coordination environment of Li in the β′ site (Fig. 1f). The other interstitial sites along the tunnel, shown in Fig. 1c,g, remain available and accessible for Li-ion insertion. While pre-intercalation does not alter the *C*2/*m* space group, in comparison with ζ-V_2O_5, the *a* unit-cell parameter is expanded and the *β* angle is compressed, resulting in an overall volume expansion of 0.76% and 2.5%[32] for Na- and K-ion pre-intercalation, respectively[23,32]. The observed larger volume expansion for the latter is readily rationalized on the basis of the larger crystal radius (1.60 Å) for seven-coordinate K^+ compared with seven-coordinate Na^+ (1.26 Å), as indicated in Fig. 1d,e. Figure 1h,i shows β-$Na_{0.25}V_2O_5$ and β-$K_{0.27}V_2O_5$ particles with a microbeam, and their structural characterizations are shown in Supplementary Fig. 2 and Supplementary Tables 7 and 8.

The electrochemical performances of β-$Na_{0.25}V_2O_5$ and β-$K_{0.27}V_2O_5$ have been contrasted by means of cyclic voltammetry and galvanostatic discharge/charge measurements (Fig. 2 and Supplementary Fig. 3). Reduction peaks at 2.78 and 2.37 V in Fig. 2a, and 2.82 and 2.44 V in Fig. 2d, are shifted to slightly higher potentials from the first to the second cycle, as a result of formation of an interface film[33–35]. In Fig. 2a,d, reduction peaks are consistent with potential slopes/plateaus in the discharge curves in Fig. 2b,e for both β-$Na_{0.25}V_2O_5$ and β-$K_{0.27}V_2O_5$. In analogy with lithiation of ζ-V_2O_5, the potential slopes/plateaus are ascribed to Li-ion reordering along the tunnels at different occupancies (see below)[29].

Figure 2b shows that the charge capacity of β-$Na_{0.25}V_2O_5$ is initially 241.5 mAh g^{-1} but is decreased to 194 mAh g^{-1} after three cycles at a *C*-rate of *C*/20. In contrast, the charge capacity of β-$K_{0.27}V_2O_5$ is initially 242 mAh g^{-1} and is essentially retained after three cycles (Fig. 2e). For comparison, the charge capacity of ζ-V_2O_5 is 228.7 mAh g^{-1} after three cycles, which is decreased from 250.9 mAh g^{-1} in the first cycle at a *C*-rate of *C*/20 (ref. 23). Upon cycling at a higher *C*-rate of *C*/2, β-$Na_{0.25}V_2O_5$ presents an initial capacity of 214.7 mAh g^{-1}, which is decreased to 196.7 mAh g^{-1} in the second cycle, and then to 187.5 mAh g^{-1} in the third cycle (Fig. 2c). In contrast, β-$K_{0.27}V_2O_5$ exhibits an initial capacity of 209.7 mAh g^{-1} at a *C*-rate of *C*/2; a capacity of 200.2 mAh g^{-1} is observed to be retained after three cycles (Fig. 2f).

Greater capacity fading at higher *C*-rates is attributable to limitations in solid-state Li-ion diffusivity, which presents a kinetic impediment to realizing the accessible insertion capacity, and further points to the need to optimize crystallite geometry, reduce particle agglomeration and identify compatible electrolytes[36–38]. On the basis of measurements of three separate cells (Supplementary Fig. 3), β-$Na_{0.25}V_2O_5$ exhibits an initial capacity of 212.9 ± 18.9 mAh g^{-1}, which is decreased to 136.3 ± 6.9 mAh g^{-1} after 50 cycles and substantially diminished to 122.5 ± 3.8 mAh g^{-1} after 100 cycles, an overall decrease of about 58%. In contrast, β-$K_{0.27}V_2O_5$ has a capacity of 202.7 ± 14.4 mAh g^{-1} in the first cycle, which decreases to 158.3 ± 7.4 mAh g^{-1} after 50 cycles and subsequently decreases to 139.4 ± 5.0 mAh g^{-1} after 100 cycles, a more modest decrease in capacity of about 30%.

Comparing long-term cycling performance of β-$Na_{0.25}V_2O_5$ and β-$K_{0.27}V_2O_5$ with that of ζ-V_2O_5, in Fig. 2g–i (Supplementary Fig. 4 shows additional datasets), ζ-V_2O_5 shows a capacity of 105 mAh g^{-1} at a *C*-rate of *C*/20 after three cycles and 78 mAh g^{-1} at *C*/5 after 100 cycles. β-$Na_{0.25}V_2O_5$ shows 115 mAh g^{-1} after three cycles and 69 mAh g^{-1} after 100 cycles. β-$K_{0.27}V_2O_5$ exhibits 220 mAh g^{-1} after three cycles and 137 mAh g^{-1} after 100 cycles, which is indeed higher than that of ζ-V_2O_5. The pre-intercalated Na ions and K ions effectively enlarge the tunnel spacing, yielding greater initial capacity. However, β-$Na_{0.25}V_2O_5$ shows lower capacity than ζ-V_2O_5 after 100 cycles, which is ascribed to the reordering of Na ions, which show a greater propensity for de-insertion. In contrast, larger K ions extensively expand the tunnel spacing and have higher migration barriers, which hold the pillaring in place, thereby boosting capacity.

The rate capacity and the kinetics of Li-ion insertion in the pre-intercalated compounds is also investigated, and inferred Li-ion diffusivities in the pre-intercalated compounds are shown (Supplementary Figs. 5–8 and Supplementary Tables 9–11). With increasing concentration of Li ions in the tunnels, Li-ion diffusivities are gradually decreased[29,39]. The Li-ion diffusivity values for β-$Na_{0.25}V_2O_5$ across intercalation regimes I–III (Supplementary Tables 9–11) generally reflect an order of magnitude enhancement compared with ζ-V_2O_5. An additional enhancement of Li-ion diffusivity is observed in the expanded tunnels of β-$K_{0.27}V_2O_5$. The enhancement in diffusivity as a result of tunnel expansion through pre-intercalation is further examined using density functional theory (DFT) simulations in subsequent sections.

To decipher the mechanistic basis for how pre-intercalation impacts electrochemical performance, we have topochemically lithiated an entire single crystal of β-$Na_{0.25}V_2O_5$. Ex situ single-crystal XRD enables Li occupancies to be examined with Ångström-level resolution—this has rarely been achieved in battery science, given the difficulties in growing and topochemically lithiating single crystals of insertion hosts with preservation of macroscopic single-crystalline domains. Compared with direct preparation of lithiated compounds wherein Li ions are ensconced in thermodynamically favoured sites, topochemical intercalation of single crystals captures electron density maps derived from Li ions traversing across the crystal lattice, and thereby allows for tracing of diffusion pathways and identification of site preferences[22,40,41]. Given the low electron density of lithium, the structure refinements have been validated through comparison of statistics from different models (Supplementary Fig. 9 and Supplementary Tables 12 and 13). Furthermore, we have used operando synchrotron powder XRD to track the dynamical evolution of structure during lithiation/delithiation. In combination, the two methods provide a comprehensive view: ex situ single-crystal diffraction affords an atomistic view of site occupancy and diffusion, whereas operando powder diffraction tracks bulk transformation under operational conditions using structure solutions from single-crystal diffraction as useful benchmarks.

Figure 3a shows the extended structure of topochemically lithiated β′-$Li_{0.33}$β-$Na_{0.32}V_2O_5$. Crystallographic refinement information is listed in Supplementary Tables 14–16. Supplementary Fig. 9 shows refinement renderings. The refined cation stoichiometries for this crystal are concordant with inductively coupled plasma mass spectrometry analysis (Supplementary Table 17). Upon chemical lithiation, in addition to an approximately 1% increase in unit-cell volume, a pronounced ordering of the Na ions is discerned along every seven-coordinated β site on one side of the tunnel, whereas Li ions segregate to every five-coordinated β′ site on the opposite side of the tunnel. This lopsided filling pattern, which alternates in adjacent tunnels, has the effect of creating a screw axis in the structure and changing the space group from *C*2/*m* to *P*21/*m*. Notably, the centring of the screw axis also changes the setting of the unit cell relative to the pristine β-$Na_{0.32}V_2O_5$ structure; consequently, the unit-cell orientation, while retaining the monoclinic lattice parameters of the pristine structure, is rotated (indicated by dashed boundaries in Fig. 3a; compare with the retained *C*2/*m* symmetry of the lithiated β-$K_{0.22}V_2O_5$ structure in Fig. 3b). These compounds

https://doi.org/10.1038/s41563-024-01842-y

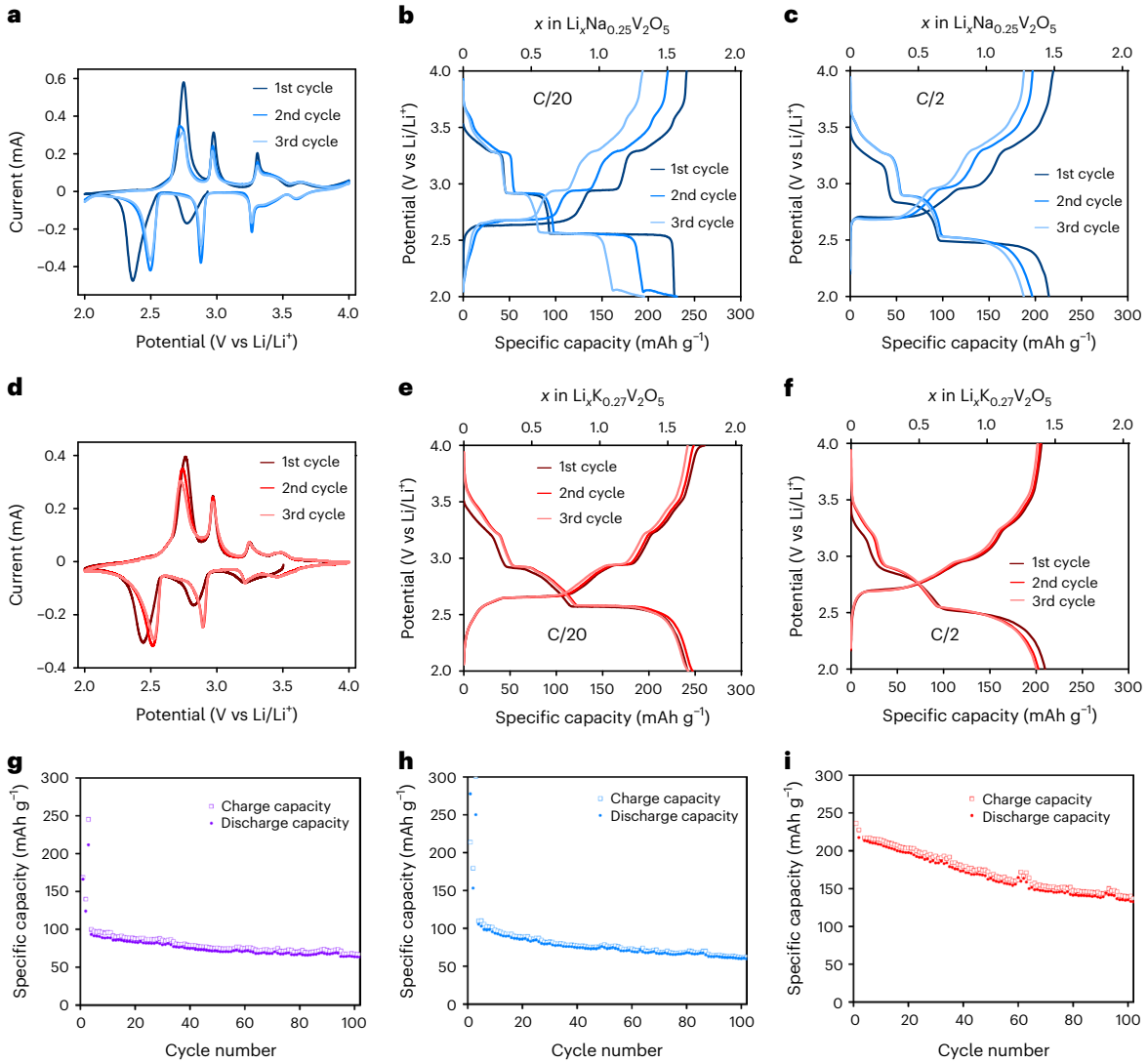

Fig. 2 | Electrochemical characterization of β-$Na_{0.25}V_2O_5$ and β-$K_{0.27}V_2O_5$. **a**,**d**, Cyclic voltammograms acquired at a scan rate of 0.1 mV s^{-1} for an initial three cycles between 2 and 4 V for β-$Na_{0.25}V_2O_5$ (**a**) and β-$K_{0.27}V_2O_5$ (**d**). **b**,**e**, Galvanostatic discharge/charge profiles acquired at a *C*-rate of *C*/20 for initial three cycles between 2 and 4 V of β-$Na_{0.25}V_2O_5$ (**b**) and β-$K_{0.27}V_2O_5$ (**e**). **c**,**f**, Galvanostatic discharge/charge profiles cycling at a *C*-rate of *C*/2 for three cycles between 2 and 4 V for β-$Na_{0.25}V_2O_5$ (**c**) and β-$K_{0.27}V_2O_5$ (**f**). **g**–**i**, Cycling performance for ζ-V_2O_5 (**g**), β-$Na_{0.25}V_2O_5$ (**h**) and β-$K_{0.27}V_2O_5$ (**i**). Cells were cycled at a *C*-rate of *C*/20 between 2.2 and 3.7 V for the first three cycles to enable electrode–electrolyte interface stabilization, followed by cycling at a rate of *C*/5 for 100 cycles. Additional cycling datasets acquired for ζ-V_2O_5, β-$Na_{0.25}V_2O_5$ and β-$K_{0.27}V_2O_5$ are presented in Supplementary Fig. 4. The greater capacity loss upon initial cycling at *C*/20 is explicable considering that stoichiometric gradients are most pronounced upon deep discharge. Consistent with this explanation, an additional voltage plateau at 2.05 V is observed after the first cycle (discharged from 4.0 to 2.0 V), which attests to greater structural distortion at the lower rate.

have been seen to exhibit supercells at low temperature[42,43], but not straight chains of β and β′ sites as reported here. Figure 3c,d shows a perspective view of the tunnels in the structure in both the pristine β-$Na_{0.32}V_2O_5$ crystal (Fig. 3c), where Na^+ ions are randomly distributed with about 50% occupancy across all available β sites, and in a crystal of the same sample that has been lithiated (Fig. 3d), where Li-ion insertion forces a rearrangement of cations. A 3D view of the extended structure is shown in Supplementary Video 1. Whereas in empty ζ-V_2O_5 all sites are equally available to Li ions and mirrored across the centre of the tunnel, pre-intercalation with Na ions bifurcates and limits Li-ion diffusion to one half of the tunnel (Fig. 3e).

Figure 3b shows a structure of β′-$Li_{0.23}$/β-$K_{0.22}V_2O_5$ that was accessed similarly by topochemical treatment of pristine β-$K_{0.22}V_2O_5$ crystals. In contrast to the distinctive cation ordering induced by Li^+ insertion in β-$Na_{0.32}V_2O_5$, the lithiated β′-$Li_{0.23}$/β-$K_{0.22}V_2O_5$ structure shows a random distribution of K and Li at the β and β′ sites, respectively (Supplementary Fig. 10 and Supplementary Tables 18–20), albeit with high site selectivity for the two cations (K ions in β sites and Li ions in β′ sites). The lithiated crystal preserves the *C*2/*m* symmetry of the parent phase in agreement with the powder XRD data in Table 1. The difference in ordering behaviour between Na and K ions on the introduction of Li ions arises from the lower mobility of K^+ and greater ionic repulsions, which prevents facile rearrangement of all ions on one side of the tunnel. The contrast between the two pre-intercalated ions highlights the potential for site-selective modification through pre-intercalation to redirect Li-ion diffusion pathways. Furthermore, topochemical transformation of a pre-intercalated single crystal highlights the versatility of this method, which has previously only been applied to crystals of empty polymorphs[22,40,41]. We posit that topochemical crystal-to-crystal transformation holds promise for generalizability to insertion hosts that undergo distortion continuously without distortive transformations.

https://doi.org/10.1038/s41563-024-01842-y

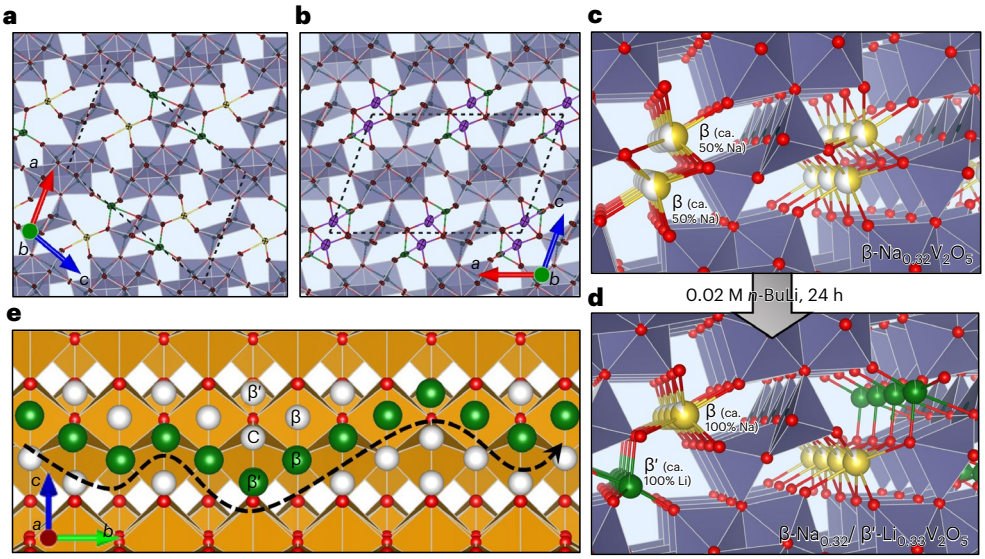

Fig. 3 | Single-crystal XRD mapping of lithium-ion diffusion in pre-intercalated β-$Na_xV_2O_5$ and β-$K_xV_2O_5$. a,**b**, View of the extended *P*21/*m* structure of topochemically lithiated β′-$Li_{0.33}$/β-$Na_{0.32}V_2O_5$ (**a**) and *C*2/*m* structure of topochemically lithiated β′-$Li_{0.23}$/β-$K_{0.22}V_2O_5$ (**b**) as refined from single-crystal XRD, viewed down the *b* axis. Colour key: yellow, Na; purple, K; green, Li; blue polyhedra, VO_6/VO_5. All thermal ellipsoids shown at 90% probability; unit-cell boundaries indicated by a dashed line. **c**,**d**, Perspective view of site-filling in the tunnel structure of β-$Na_{0.32}V_2O_5$ before (**c**) and after (**d**) topochemical lithiation with 0.02 M *n*-BuLi, showing the reordering of Na^+ ions (yellow) from random distribution in all β sites to only half of β sites on one side of the tunnel, to accommodate Li^+ ions (green) in half of β′ sites on the opposite side. Partial atomic occupancy as obtained from single-crystal refinement is indicated by the partial filling of spheres and by site labels. **e**, View of Li-ion diffusion through an empty ζ-V_2O_5 tunnel, as viewed in cutaway down the *a* axis, showing the unrestricted access to β, β′ and C sites mirrored across the centre of the tunnel in contrast to the lopsided filling motif obtained by lithiation of pre-intercalated β-$Na_xV_2O_5$. Available sites are indicated by colourless spheres, sites filled by Li^+ along a hypothetical diffusion pathway are coloured green and the pathway is indicated by a dashed arrow.

Table 1 | Lattice parameters corresponding to each of the insertion regimes for β-$Na_{0.25}V_2O_5$ and β-$K_{0.27}V_2O_5$ during electrochemical lithiation as deduced from operando synchrotron powder XRD measurements (related in Fig. 4)

	x in $Li_xM_yV_2O_5$	Regime	Potential (V)	*a* (Å)	*b* (Å)	*c* (Å)	*β* (°)	*V* (Å^3)	Space group
β-$Na_{0.25}V_2O_5$	0	A	3.66	15.409	3.609	10.078	109.541	528.168	*C*2/*m*
	0 < x ≤ 0.4	B	3.66-3.06	15.358	3.627	10.158	109.639	532.956	*C*2/*m*
	0.4 < x ≤ 0.8	C	3.06-2.53	15.358	3.627	10.158	109.639	532.956	*C*2/*m*
				15.330	3.674	10.312	112.218	537.734	*C*2/*m*
	0.8 < x ≤ 1.7	D	2.53–2.0	15.330	3.674	10.312	112.218	537.734	*C*2/*m*
				15.189	3.881	10.017	105.14	570.097	*P*2/*m*
β-$K_{0.27}V_2O_5$	0	A′	3.63	15.608	3.612	10.093	109.302	537.085	*C*2/*m*
	0 < x ≤ 0.3	B′	3.63-3.15	15.660	3.617	10.118	110.740	535.913	*C*2/*m*
	0.3 < x ≤ 0.8	C′	3.15-2.60	15.660	3.617	10.118	110.740	535.913	*C*2/*m*
				14.945	3.942	9.921	106.379	560.744	*P*2/*m*
	0.8 < x ≤ 1.7	D′	2.60-2.0	14.945	3.942	9.921	106.379	560.744	*P*2/*m*
				15.627	3.703	9851	103.05	555.402	*P*21

The specific interstitial sites occupied by Li ions within the tunnels of β-$Na_{0.25}V_2O_5$ and β-$K_{0.27}V_2O_5$ have been inferred from single-crystal XRD studies of chemically prepared single crystals of β/β′-$Li_xV_2O_5$[22] (Fig. 1c) and lithiated β-$Na_{0.25}V_2O_5$/β-$K_{0.22}V_2O_5$ as shown in Fig. 3 and Supplementary Fig. 10.

We next turn our attention to operando synchrotron powder XRD studies. The discharge/charge profiles of β-$Na_{0.25}V_2O_5$ and β-$K_{0.27}V_2O_5$ in Fig. 4a and f exhibit potential slopes/plateaus that are entirely consistent with those in Fig. 2b and e, respectively. In addition, the corresponding contour plots in Fig. 4b and g indicate that the lithiation/delithiation processes are reversible for both β-$Na_{0.25}V_2O_5$ and β-$K_{0.27}V_2O_5$. The lattice parameters are obtained as the function of the extent of lithiation, as shown in Table 1. The local vanadium coordination in β-$M_xV_2O_5$ is remarkably stable with respect to changes in the identity and concentration of intercalated ions; the V_2O_5 host lattice can be considered to be constituted from rigid VO_x polyhedra connected by flexible V–O–V joints. It is the flexibility of these bond angles that allows the unit cell to expand or contract while preserving overall V–O connectivity. Cation insertion and pre-intercalation have a marked impact on the symmetry of the structures, which adopt different space groups during continuous transformation that can be observed in the appearance/disappearance of new reflections in the powder XRD patterns shown in Fig. 4. However, these changes in symmetry do not result from flexions around polyhedral lattices, but are entirely attributable to rearrangement of Li, Na and K cations in the ζ-V_2O_5 tunnels.

https://doi.org/10.1038/s41563-024-01842-y

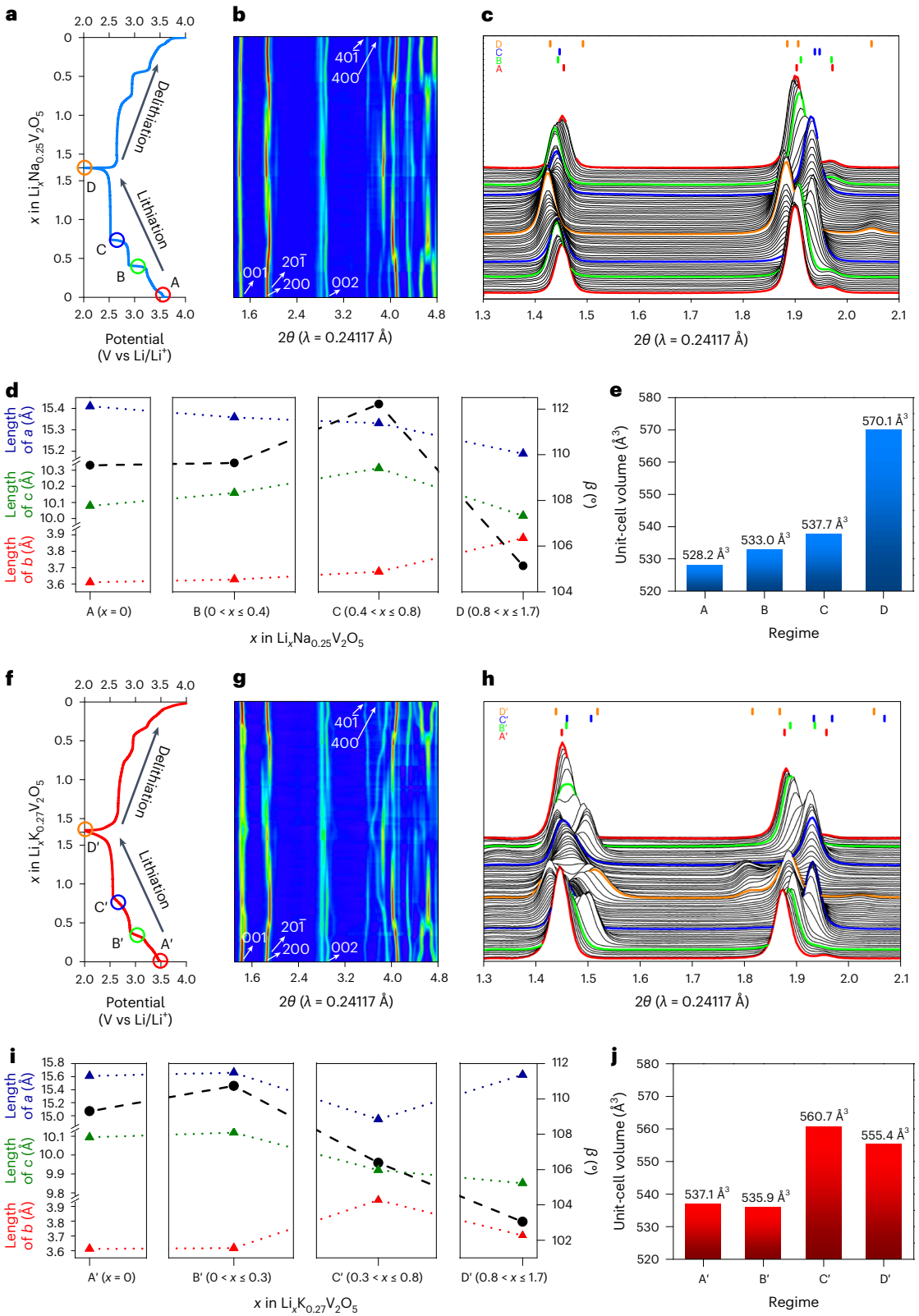

Fig. 4 | Structural evolution characterized by operando synchrotron powder XRD. a,**f**, Galvanostatic discharge/charge profiles acquired during operando powder XRD measurements at a *C*-rate of *C*/20 for the first cycle between 2 and 4 V for β-$Na_{0.25}V_2O_5$ (**a**) and β-$K_{0.27}V_2O_5$ (**f**). **b**,**g**, Operando powder XRD contour plots of β-$Na_{0.25}V_2O_5$ (**b**) and β-$K_{0.27}V_2O_5$ (**g**), which correspond to discharge/charge processes in **a** and **f**. **c**,**h**, Corresponding magnified view of operando powder XRD waterfall plots in the range of $2\theta = 1.3–2.1°$ during discharge/charge of β-$Na_{0.25}V_2O_5$ (**c**) and β-$K_{0.27}V_2O_5$ (**h**). **d**,**i**, Lattice parameters *a* (blue triangles), *b* (red triangles), *c* (green triangles) and *β* (black circles) of β-$Na_{0.25}V_2O_5$ (**d**) and β-$K_{0.27}V_2O_5$ (**i**). **e**,**j**, Unit-cell volume comparison in corresponding regimes of β-$Na_{0.25}V_2O_5$ (**e**) and β-$K_{0.27}V_2O_5$ (**j**). A, B, C and D correspond to intercalation regimes for β-$Na_{0.25}V_2O_5$ and A′, B′, C′ and D′ to intercalation regimes for β-$K_{0.27}V_2O_5$, which are listed in Table 1.

https://doi.org/10.1038/s41563-024-01842-y

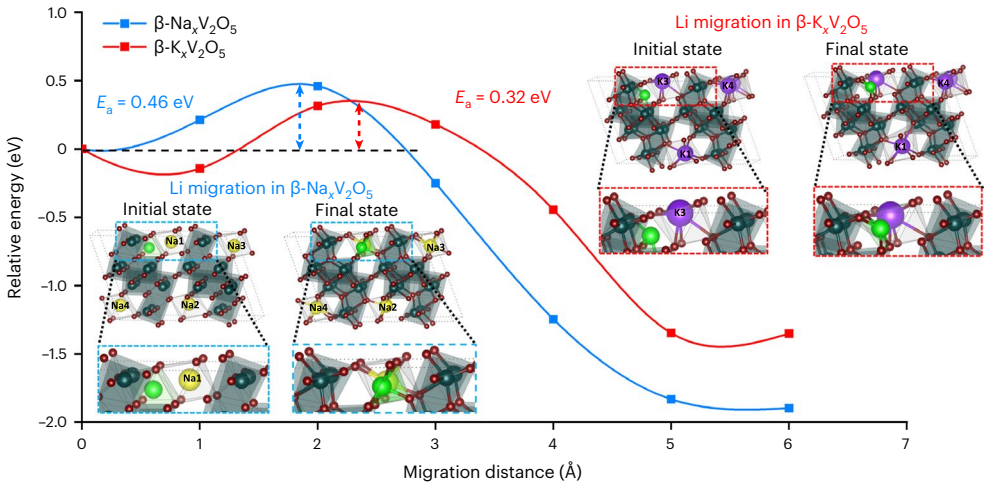

Fig. 5 | Migration barriers in pre-intercalated compounds. Relative energy barrier representations calculated for Li-ion migration within pre-intercalated β-$Na_xV_2O_5$ and β-$K_xV_2O_5$. Blue and red curves depict Li migration pathways and barriers in pre-intercalated β-$Na_xV_2O_5$ and β-$K_xV_2O_5$, respectively. Li, Na, K, O and V atoms are represented by green, yellow, purple, red and dark-blue spheres, respectively.

For both β-$Na_{0.25}V_2O_5$ and β-$K_{0.27}V_2O_5$, during the discharging process, initial Li-ion intercalation slightly expands the tunnel structure ascribed to Li ions occupying β′ sites (Fig. 3d, Fig. 4, Supplementary Fig. 10 and Supplementary Video 1). With further lithiation, the symmetry of the structure ($0.4 < x \leq 0.8$, x in $Li_xNa_{0.25}V_2O_5$) is maintained but with expansion of the tunnel, evidenced by an increase of the unit-cell volume to 537.73 Å^3 and increased distortion of the monoclinic β angle to 112.218°, which corresponds to a highly lithiated ζ-V_2O_5 structure where β and β′ sites are both occupied and C sites begin filling[22]. For the structure β-$K_{0.27}V_2O_5$ ($0.3 < x < 0.8$, x in $Li_xK_{0.27}V_2O_5$), a splitting of the 001 reflection is observed in Fig. 4h, indicating a reduction in symmetry to a *P*2/*m* space group as inserted Li ions begin to fill β sites between pre-intercalated K ions. Further lithiation to 2.0 V ($0.8 < x \leq 1.7$, x in $Li_xNa_{0.25}V_2O_5$) results in the unit-cell volume being expanded to 570.097 Å^3 and β being changed to 105.14° with the lower symmetry of the *P*2/*m* space group. This regime corresponds to Li ions occupying the remaining complement of β sites[22,23].

With still further Li-ion intercalation down to 2.0 V, the volume of the lithiated β-$K_{0.27}V_2O_5$ structure shrinks to 555.402 Å^3 and the symmetry of the unit cell is reduced still further to the *P*21 space group. Consistent with Fig. 3d and Supplementary Fig. 10, the stoichiometry corresponds to filling β′, C and β sites, and probably additional sites that become available as a result of tunnel expansion. During the charging process, both lithiated structures readily revert from *P*2/*m* to *C*2/*m*, and then finally to the pristine β-$Na_{0.25}V_2O_5$, illustrating complete preservation of the 1D tunnel framework.

A discontinuous change in unit-cell volume is observed when Li ions begin to occupy β sites[22] between the pre-intercalated Na and K ions and is clearly discernible in discharge curves. For both β-$Na_{0.25}V_2O_5$ and β-$K_{0.27}V_2O_5$, lithiation/delithiation is entirely reversible[26,44]. In the latter compound, a series of lower-symmetry structures becomes accessible upon increasing lithiation, probably as a result of new sites that become accessible in the expanded tunnel, enabling higher accessible capacity. While pre-intercalated Na and K ions occupy a fraction of sites that would otherwise have been accessible for Li ions, the expanded tunnels enable a higher accessible capacity and improved Li-ion diffusivity compared with ζ-V_2O_5. It is worth noting that pre-intercalation is not a universal design strategy. In more rigid insertion hosts, pre-intercalation can occlude otherwise favourable diffusion pathways or increase the likelihood of framework anion migration and structural collapse.

On the basis of DFT simulations, Fig. 5 sketches the Li-ion migration pathway in pre-intercalated $Na_xV_2O_5$ and $K_xV_2O_5$ along the crystallographic *b* direction, which corresponds to activation energy barriers of 0.46 and 0.32 eV, respectively. These results are concordant with greater Li-ion diffusivities measured in β-$K_xV_2O_5$ compared with β-$Na_xV_2O_5$ (Supplementary Figs. 5–8 and Supplementary Tables 9–11). A lower activation energy barrier for Li-ion diffusion in β-$K_xV_2O_5$ is attributable to the greater size of K ions compared with Na ions, which leads to greater tunnel expansion. Supplementary Fig. 11 shows a comparison with empty ζ-V_2O_5 and β-$Li_xV_2O_5$ respectively. The barrier to Li-ion migration in empty ζ-V_2O_5 is only about 0.14 eV, whereas for a relatively filled tunnel the migration barrier rises to about 0.54 eV. Supplementary Figs. 12 and 13 plot total and projected density of states. Pre-intercalation leads to vanadium reduction, which gives polaronic states at the top of the valence band; such states further enhance electrical conductivity compared with the empty ζ-V_2O_5 polymorph.

In conclusion, a combination of (1) topochemical lithiation tracked by ex situ single-crystal diffraction and (2) operando synchrotron powder XRD evaluation of electrochemical lithiation of pre-intercalated β-$Na_{0.25}V_2O_5$ and β-$K_{0.27}V_2O_5$ provides mechanistic understanding of the structural role of pre-intercalation in providing access to a higher reversible capacity and improved Li-ion diffusivity. The pre-intercalated alkali-metal ions occupy β sites within expanded tunnels; this tunnel expansion alleviates repulsive Coulombic interactions amongst inserted Li ions and yields more expansive transition states for site-to-site Li-ion diffusion. Pre-intercalation with Na ions results in remarkable segregation of Na and Li ions across opposite sides of the tunnel. Individual 'lanes' are not observed upon K-ion pre-intercalation, wherein Li-ion migration nevertheless proceeds with high selectivity towards β′ and C sites. Whilst pre-intercalation 'sacrifices' a fraction of interstitial sites that would have otherwise been occupied by Li ions, the results demonstrate that the tunnel expansion propping-open effect more than compensates for this by providing access to a higher accessible capacity, enabling higher Li-ion diffusivity, and exhibiting greater capacity retention. The results demonstrate the structural basis for unlocking greater reversible capacity and enhanced Li-ion diffusivity through site-selective modification of a promising intercalation host. Future work will focus on optimization of particle geometries and design of 3D mesoscale architectures that alleviate kinetic impediments and permit more effective utilization of the active material[6,45–47]. Surface coatings, systematic alloying and electrolyte optimization are also necessary to increase capacity retention.

Online content

Any methods, additional references, Nature Portfolio reporting summaries, source data, extended data, supplementary information, acknowledgements, peer review information; details of author contributions and competing interests; and statements of data and code availability are available at https://doi.org/10.1038/s41563-024-01842-y.

References

1. Cano, Z. P. et al. Batteries and fuel cells for emerging electric vehicle markets. *Nat. Energy* **3**, 279–289 (2018).
2. Goodenough, J. B. & Park, K. S. The Li-ion rechargeable battery: a perspective. *J. Am. Chem. Soc.* **135**, 1167–1176 (2013).
3. Whittingham, M. S. Lithium batteries: 50 years of advances to address the next 20 years of climate issues. *Nano Lett.* **20**, 8435–8437 (2020).
4. Whittingham, M. S., Siu, C. & Ding, J. Can multielectron intercalation reactions be the basis of next generation batteries? *Acc. Chem. Res.* **51**, 258–264 (2018).
5. Ryan, E. M. & Mukherjee, P. P. Mesoscale modeling in electrochemical devices—a critical perspective. *Prog. Energy Combust. Sci.* **71**, 118–142 (2019).
6. Luo, Y. et al. Effect of crystallite geometries on electrochemical performance of porous intercalation electrodes by multiscale operando investigation. *Nat. Mater.* **21**, 217–227 (2022).
7. Zhao, Y. et al. A review on modeling of electro-chemo-mechanics in lithium-ion batteries. *J. Power Sources* **413**, 259–283 (2019).
8. Whittingham, M. S. Lithium batteries and cathode materials. *Chem. Rev.* **104**, 4271–4301 (2004).
9. Manthiram, A. A reflection on lithium-ion battery cathode chemistry. *Nat. Commun.* **11**, 1550 (2020).
10. Liu, L. et al. Alkali ions pre-intercalated layered MnO_2 nanosheet for zinc-ions storage. *Adv. Energy Mater.* **11**, 2101287 (2021).
11. Clites, M. & Pomerantseva, E. Bilayered vanadium oxides by chemical pre-intercalation of alkali and alkali-earth ions as battery electrodes. *Energy Storage Mater.* **11**, 30–37 (2018).
12. Liu, G. et al. K^+ pre-intercalated manganese dioxide with enhanced Zn^{2+} diffusion for high rate and durable aqueous zinc-ion batteries. *J. Mater. Chem. A* **7**, 20806–20812 (2019).
13. Chernova, N. A., Roppolo, M., Dillon, A. C. & Whittingham, M. S. Layered vanadium and molybdenum oxides: batteries and electrochromics. *J. Mater. Chem.* **19**, 2526–2552 (2009).
14. Kumagai, N., Tanno, K., Nakajima, T. & Watanabe, N. Structural changes of Nb_2O_5 and V_2O_5 as rechargeable cathodes for lithium battery. *Electrochim. Acta* **28**, 17–22 (1983).
15. Santos, D. A., Dixit, M. K., Pradeep Kumar, P. & Banerjee, S. Assessing the role of vanadium technologies in decarbonizing hard-to-abate sectors and enabling the energy transition. *iScience* **24**, 103277 (2021).
16. De Jesus, L. et al. Lithiation across interconnected V_2O_5 nanoparticle networks. *J. Mater. Chem. A* **5**, 20141–20152 (2017).
17. Parija, A. et al. Topochemically de-intercalated phases of V_2O_5 as cathode materials for multivalent intercalation batteries: a first-principles evaluation. *Chem. Mater.* **28**, 5611–5620 (2016).
18. Horrocks, G. A. et al. Mitigating cation diffusion limitations and intercalation-induced framework transitions in a 1D tunnel-structured polymorph of V_2O_5. *Chem. Mater.* **29**, 10386–10397 (2017).
19. De Jesus, L. R., Andrews, J. L., Parija, A. & Banerjee, S. Defining diffusion pathways in intercalation cathode materials: some lessons from V_2O_5 on directing cation traffic. *ACS Energy Lett.* **3**, 915–931 (2018).
20. Luo, Y. et al. Roadblocks in cation diffusion pathways: implications of phase boundaries for Li-ion diffusivity in an intercalation cathode material. *ACS Appl. Mater. Interfaces* **10**, 30901–30911 (2018).
21. De Jesus, L. R. et al. Mapping polaronic states and lithiation gradients in individual V_2O_5 nanowires. *Nat. Commun.* **7**, 12022 (2016).
22. Handy, J. V., Luo, Y., Andrews, J. L., Bhuvanesh, N. & Banerjee, S. An atomic view of cation diffusion pathways from single-crystal topochemical transformations. *Angew. Chem. Int. Ed.* **59**, 16385–16392 (2020).
23. Luo, Y. et al. Cation reordering instead of phase transitions: origins and implications of contrasting lithiation mechanisms in one-dimensional (1D) ζ- and two-dimensional (2D) α-V_2O_5. *Proc. Natl Sci. USA* e2115072119 (2022).
24. Wadsley, A. D. The crystal structure of $Na_{2-x}V_6O_{15}$. *Acta Crystallogr.* **8**, 695–701 (1955).
25. Clites, M. & Pomerantseva, E. Stabilization of battery electrodes through chemical pre-intercalation of layered materials. *Low-Dimens. Mater. Devices* **9924**, 992405 (2016).
26. Chen, L. et al. Guest ions pre-intercalation strategy of manganese-oxides for supercapacitor and battery applications. *J. Energy Chem.* **60**, 480–493 (2021).
27. Mitchell, J. B. et al. Confined interlayer water promotes structural stability for high-rate electrochemical proton intercalation in tungsten oxide hydrates. *ACS Energy Lett.* **4**, 2805–2812 (2019).
28. Galy, J., Darriet, J., Casalot, A. & Goodenough, J. B. Structure of the MxV_2O and MxV_2-YTO_5 phases. *J. Solid State Chem.* **1**, 339–348 (1970).
29. Baddour-Hadjean, R., Bach, S., Emery, N. & Pereira-Ramos, J. P. The peculiar structural behaviour of β-$Na_{0.33}V_2O_5$ upon electrochemical lithium insertion. *J. Mater. Chem.* **21**, 11296–11305 (2011).
30. Krogstad, M. J. et al. Reciprocal space imaging of ionic correlations in intercalation compounds. *Nat. Mater.* **19**, 63–68 (2020).
31. Bach, S., Pereira-Ramos, J. P., Baffier, N. & Messina, R. A thermodynamic and kinetic study of electrochemical lithium intercalation in $Na_{0.33}V_2O_5$ bronze prepared by a sol–gel process. *J. Electrochem. Soc.* **137**, 1042–1048 (1990).
32. Andrews, J. L. et al. Reversible Mg-ion insertion in a metastable one-dimensional polymorph of V_2O_5. *Chem* **4**, 564–585 (2018).
33. Li, J. et al. Phase evolution of conversion-type electrode for lithium ion batteries. *Nat. Commun.* **10**, 2224 (2019).
34. Varghese, B. et al. Fabrication of NiO nanowall electrodes for high performance lithium ion battery. *Chem. Mater.* **20**, 3360–3367 (2008).
35. He, C. et al. Carbon-encapsulated Fe_3O_4 nanoparticles as a high-rate lithium ion battery anode material. *ACS Nano* **7**, 4459–4469 (2013).
36. Wang, G. et al. Mesoporous $LiFePO_4$/C nanocomposite cathode materials for high power lithium ion batteries with superior performance. *Adv. Mater.* **22**, 4944–4948 (2010).
37. Luo, J. Y., Wang, Y. G., Xiong, H. M. & Xia, Y. Y. Ordered mesoporous spinel $LiMn_2O_4$ by a soft-chemical process as a cathode material for lithium-ion batteries. *Chem. Mater.* **19**, 4791–4795 (2007).
38. Hu, J. et al. 3D-printed cathodes of $LiMn_{1-x}Fe_xPO_4$ nanocrystals achieve both ultrahigh rate and high capacity for advanced lithium-ion battery. *Adv. Energy Mater.* **6**, 1600856 (2016).
39. Pereira-Ramos, J. P., Messina, R., Znaidi, L. & Baffier, N. Electrochemical lithium intercalation in $Na_{0.33}V_2O_5$ bronze prepared by sol–gel processes. *Solid State Ion.* **28–30**, 886–894 (1988).
40. Handy, J. V. et al. A 'Li-eye' view of diffusion pathways in a 2D intercalation material from topochemical single-crystal transformation. *ACS Energy Lett.* **7**, 1960–1962 (2022).
41. Handy, J. V. et al. Topochemical stabilization and single-crystal transformations of a metastable 2D γ′-V_2O_5 intercalation cathode. *Cell Rep. Phys. Sci.* **3**, 100712 (2022).

42. Yamada, H. & Ueda, Y. Magnetic electric and structural properties of β-$A_xV_2O_5$ (A = Na, Ag). *J. Phys. Soc. Jpn.* **68**, 2735–2740 (1999).
43. Chen, B. et al. Electronic structure of β-$Na_xV_2O_5$($x \approx 0.33$) polycrystalline films: growth spectroscopy and theory. *J. Phys. Chem. C* **118**, 1081–1094 (2014).
44. Xu, Y., Han, X., Zheng, L., Yan, W. & Xie, Y. Pillar effect on cyclability enhancement for aqueous lithium ion batteries: a new material of β-vanadium bronze $M_{0.33}V_2O_5$ (M = Ag, Na) nanowires. *J. Mater. Chem.* **21**, 14466–14472 (2011).
45. Rajendra, T. et al. Quantifying transport, geometrical, and morphological parameters in Li-ion cathode phases using X-ray microtomography. *ACS Appl. Mater. Interfaces* **11**, 19933–19942 (2019).
46. Andrews, J. L. et al. Curvature-induced modification of mechano-electrochemical coupling and nucleation kinetics in a cathode material. *Matter* **3**, 1754–1773 (2020).
47. Schulze, M. C., Belson, R. M., Kraynak, L. A. & Prieto, A. L. Electrodeposition of Sb/CNT composite films as anodes for Li- and Na-ion batteries. *Energy Storage Mater.* **25**, 572–584 (2020).

Methods

Growth of single crystals of β-$Na_xV_2O_5$ and β-$K_xV_2O_5$

As reported previously[48], powders of the intercalated β-$M_xV_2O_5$ species were synthesized from stoichiometric amounts of $Na_2C_2O_4$ (≥99.5%, Sigma-Aldrich) or $K_2C_2O_4$ (≥99.5%, Sigma-Aldrich) and α-V_2O_5 powder (≥99.6%, Alfa Aesar) that were ball-milled (SPEX mill, acrylic beads) for 2 h and then annealed in alumina boats under argon atmosphere at 550 °C for 24 h. Single crystals were obtained by ball-milling these powders a second time, and then sealing the powders in evacuated quartz ampoules, melting at 800 °C and slow-cooling through the melting point at a rate of 2 °C h^{-1}. This method yielded large, lustrous black crystals with a plate-like habit.

Topochemical lithiation of β-$Na_{0.32}V_2O_5$ and β-$K_{0.22}V_2O_5$ single crystals

After high-quality crystals in the desired stoichiometric range had been identified, about 5 mg of pristine crystals were topochemically lithiated with retention of the original crystal lattice by immersion for 24 h in 10 ml of *n*-butyllithium solution (Sigma-Aldrich, 2.5 M in hexanes) diluted with heptanes, to concentrations of 0.02 M and 0.033 M for β-$Na_{0.32}V_2O_5$ and β-$K_{0.22}V_2O_5$, respectively. The potential of *n*-BuLi is estimated to be about 1.0 V versus Li^+/Li[49]. After topochemical treatment at these concentrations, crystals retained their black, plate-like habit with minimal damage and cracking, probably due to pre-intercalated cations acting as a structural buttress for the tunnel.

Synthesis of ζ-V_2O_5 powder

As reported previously[23], V_2O_5 (≥98%, Sigma-Aldrich) and silver acetate were dispersed in deionized water (resistivity, ρ = 18.2 MΩ cm^{-1}) and then reacted hydrothermally at 210 °C for 5 d. After being washed with a large amount of water and isopropanol, the obtained β-$Ag_{0.33}V_2O_5$ powder was reacted with hydrochloric acid solution to leach Ag^+. ζ-V_2O_5 was obtained after washing with a 10 wt% aqueous solution of sodium thiosulfate and deionized water.

Synthesis of β-$Na_{0.25}V_2O_5$ and β-$K_{0.27}V_2O_5$ powders

In a typical synthesis, 1.82 g orthorhombic V_2O_5 (≥98%, Sigma-Aldrich) and 2.7 g oxalic acid (≥98%, Sigma-Aldrich) were dispersed in 100 ml deionized water (ρ = 18.2 MΩ cm^{-1}) in a beaker, which was placed on a heating plate held at 80 °C. The dispersion was vigorously stirred using a magnetic stirrer. After the solution turned deep blue in colour, the alkali-metal nitrate salt (0.2125 g $NaNO_3$ or 0.2730 g KNO_3) was added to the blue solution and vigorously stirred in the open air until free water was evaporated and sponge-textured dark-brown powder was obtained. The recovered solid was then ground using a mortar and pestle and annealed under ambient conditions in a muffle furnace at 450 °C for 6 h.

Ex situ single-crystal diffraction

Single-crystal diffraction data were collected on a Bruker Quest X-ray diffractometer utilizing the APEX3 software suite, with X-ray radiation generated from a Mo-Iμs X-ray tube (K_α = 0.71073 Å). All crystals were placed in a cold N_2 stream maintained at 110 K. Four different single crystals of β-$Na_{0.32}V_2O_5$ were solved and do not show any evidence of segregation/supercell ordering before Li-ion insertion. A second, separately lithiated β-$Na_xV_2O_5$ crystal exhibited the same Li- and Na-ion ordering pattern upon structure solution and refinement.

Following unit-cell determination, extended data collection was performed using omega and phi scans. Data reduction, integration of frames, merging and scaling were performed with the program APEX3, and absorption correction was performed utilizing the program SADABS. Structures were solved using intrinsic phasing, and least-squares refinement for all structures was carried out using the square of the structure factors. Structural refinement and the calculation of derived results were performed using the SHELXTL package of computer programs and ShelXle[50,51]. Detailed refinement and crystal information is provided in Supplementary Tables 1–6, 14–16 and 18–20. Crystallographic Information Files corresponding to β-$Na_{0.32}V_2O_5$ and β-$K_{0.22}V_2O_5$ used in this study, as well as to the new structures β-$Na_{0.32}$/β′-$Li_{0.33}V_2O_5$ and β′-$Li_{0.23}$/β-$K_{0.22}V_2O_5$, have been deposited in the Cambridge Structural Database and are available for access with deposition numbers 2150932, 2150933, 2150934 and 2203830, respectively.

We have systematically ruled out the possibility of a misassignment of Li atoms arising from Fourier series truncation or incorrect phase estimation during refinement. Notably, these errors tend to accumulate near heavy atoms or at high-symmetry positions. However, the electron density peaks (*Q*-peaks) corresponding to Li atoms are at the farthest remaining position from other atoms (in the tunnel interstices), and are indeed not in proximity to any of the special positions (that is, the intersections of twofold rotations in *C*2/*m* structures or 2_1 screw axes in $P2_1/m$ structures with the mirror planes on which all atoms in the structure reside). Finally, assigning the β′ sites as a partial occupancy Li atom improves the refinement residual, as validated by performing structure refinements of the chemically lithiated crystals both with and without assignment of the β′-site *Q*-peak. Tabulated refinement statistics and images of the unit cells are shown in Supplementary Table 13 and Supplementary Fig. 9. Both R1 and wR2 residual scores are greatly improved by Li-ion assignment. Without lithium assigned, the β′-site *Q*-peak is the largest in the structure, and upon assignment the next-highest *Q*-peak is located near a V site and is probably a Fourier series truncation error. Finally, we note that chemical lithiation of single crystals of β-$Na_{0.32}V_2O_5$ and β-$K_{0.22}V_2O_5$ modifies not just electron density but also both the lattice parameters and lattice volume, as illustrated in Supplementary Table 12.

Morphological characterization

SEM was conducted on a JEOL JSM-7500F FE-SEM operated at an accelerating voltage of 5 kV.

Electrochemical characterization

CR2032 coin cells were prepared in a glovebox filled with Ar. The working electrode was prepared by casting the mixture of the active material (ζ-V_2O_5, β-$Na_{0.25}V_2O_5$ or β-$K_{0.27}V_2O_5$, 70 wt%), conductive carbon (Super C45, 20 wt%) and binder (poly(vinylidene fluoride), 10 wt%) dispersed in *N*-methyl-2-pyrrolidone onto an Al foil substrate, following by drying at 70 °C in a forced air oven. The counter-electrode and separator were lithium metal and Celgard 2500, respectively. The electrolyte was 1 M $LiPF_6$ in a solvent mixture of ethylene carbonate and diethyl carbonate with a volume ratio of 1:1. The cells were galvanostatically discharged and charged in a voltage range of 2–4 V using a LANHE (CT2001A) battery testing system. Cyclic voltammetry measurements were performed using a Bio-Logic electrochemical potentiostat in the voltage range of 2–4 V. To determine Li-ion diffusivities, cyclic voltammetry was performed at different scan rates.

Li-ion diffusivities (D_{Li^+}) can be extrapolated by using the Randles–Sevcik equation[52,53]:

$$i_p = \left(2.69 \times 10^5\right) n^{3/2} S D_{Li^+}^{1/2} C_{Li}^{*} v^{1/2} \quad (1)$$

where i_p represents the peak current at reduction/oxidation states, *n* is the number of electrons transferred in the redox reaction, *S* refers to the area of the electrode (cm^2), C_{Li}^{*} is the concentration of Li ions (mol cm^{-3}) and *v* is the scan rate used in the experiment.

Galvanostatic intermittent titration technique experiments were confirmed to examine the Li-ion diffusivities as functions of state of discharge/charge. This technique is based on the assumption of 1D diffusion in a solid-solution electrode and also assumes a uniform current distribution throughout the electrode. The reaction between the electrode surface and electrolyte is not explicitly considered[54]. In galvanostatic intermittent titration technique measurements, a small

constant current at a *C*-rate of *C*/20 was applied for 20 min, followed by a rest time of 2 h to allow the cell voltage to reach its steady-state value, then the change of potential was measured to extract the Li-ion diffusion coefficient as per ref. 55:

$$D_{Li^+} = \frac{4}{\pi\tau}\left(\frac{m_B V_m}{M_B A}\right)^2\left(\frac{\Delta E_s}{\Delta E_\tau}\right)^2 (\tau \ll L^2/D_{Li^+}) \quad (2)$$

where m_B is the mass of active material in an electrode, V_m is the molar volume of the active material, M_B is the molecular weight of the active material, A is the area of an electrode, ΔE_s and ΔE_τ are the potential difference, τ is the duration of the current pulse and L is the thickness of electrode as shown in Supplementary Fig. 6.

Furthermore, electrochemical impedance spectroscopy has been used to examine the Li-ion diffusion coefficient because it provides kinetic information that can be related to a specific state of charge or discharge. This measurement is made by applying a low-amplitude signal around an equilibrium state at three oxidation/reduction reaction potentials in the frequency range of 0.01–10,000 Hz. Each Nyquist plot includes a high-frequency semicircle and Warburg tail region. The high-frequency semicircle corresponds to charge-transfer resistance relevant to interfacial Li-ion transfer. The Warburg tail region is related to Li-ion diffusion in the active material[56]. The real component of the resistance has been plotted versus the inverse square root of the angular speed in the low-frequency range; the Warburg factor (σ) is determined from the slope. The lithium diffusion coefficient is inferred from[57]

$$D_{Li^+} = \frac{R^2T^2}{2A^2n^4F^4C^2\sigma^2} \quad (3)$$

where R is the gas constant, T is the absolute temperature, F is Faraday's constant and C is the molar concentration of Li ions in an active material.

For long-term cycling measurements, the electrodes were prepared by mixing the active material (ζ-V_2O_5, β-$Na_{0.25}V_2O_5$ or β-$K_{0.27}V_2O_5$, 80 wt%) with conductive carbon (Super P C45, MSE Supplies, 10 wt%) and binder (poly(vinylidene fluoride), 10 wt%). The composite was added to *N*-methyl-2-pyrrilodone (NMP) solvent and mixed using a high-shear mixer to create a homogeneous slurry. Subsequently, the slurry mixture was laminated onto a carbon-coated aluminium foil current collector (MTI Corporation) and dried to remove NMP. Dried electrodes with an area of 1.32 cm^2 contained 9–15 mg of active material and were assembled in CR2032 coin cells in an Ar-filled glovebox. Lithium metal chips were used as the counter-electrode and Celgard 2320 as the separator. The electrolyte was a solution of 1 M $LiPF_6$ in a solvent mixture of ethylene carbonate and ethyl methyl carbonate with a volume ratio of 1:1. The cells were charged under constant current constant voltage and discharged under constant current. All coin cells were cycled at a *C*-rate of *C*/20 between 2.2 and 3.7 V for the first three cycles for electrode–electrolyte interface stabilization, followed by cycling at a *C*-rate of *C*/5 for 100 cycles.

Operando synchrotron powder XRD

Electrodes for operando powder XRD studies were constructed by mixing carbon black (Vulcan XC-72, Cabot Corporation), graphite (300 mesh, 99%, Alfa Aesar), polytetrafluoroethylene binder (Sigma-Aldrich) and as-prepared β-$Na_{0.25}V_2O_5$ or β-$K_{0.27}V_2O_5$ in a ratio of 7.5:7.5:15:70 (w/w/w/w) using a mortar and pestle. The mixture was pressed into a 10-mm-diameter pellet as the working electrode. Lithium metal (Sigma-Aldrich) and glass fibre were used as the reference electrode and separator, respectively. The electrolyte was 1 M $LiPF_6$ in a solvent mixture of ethylene carbonate and diethyl carbonate with a volume ratio of 1:1. The AMPIX cell, which replicates a coin cell configuration but is equipped with Kapton tape protecting the glassy carbon X-ray transmissive windows, was assembled in a glovebox under an argon atmosphere to enable operando studies[58]. Operando synchrotron powder XRD was performed at beamline 17-BM-B at the Advanced Photon Source using a wavelength of 0.24117 Å with an amorphous silicon flat panel detector.

Synchrotron X-ray datasets were analysed using GSAS II, an open-source crystallography package[59]. Two-dimensional images were masked and integrated using a LaB_6 standard for calibration. Background scans were performed on cells with the negative electrode, electrolyte and separator but without a positive electrode. Rietveld refinements and Pawley refinements were performed to evaluate the lattice parameters on the basis of structural models derived from the Inorganic Crystal Structural Database as well as single-crystal structure solutions reported here.

Computational methodology

Transition pathway predictions were performed on the basis of the climbing image nudged elastic band method[60], within the framework of the DFT formalism[61,62], as implemented in the Vienna Ab Initio Simulation Package[63]. The projector-augmented-wave[64] formalism has been used for electronic structure calculations; the generalized gradient approximation[65] along with a Hubbard U parameter has been used to treat delocalization of 3*d* electrons of vanadium. A converged plane-wave basis set with a 500 eV kinetic energy cut-off with 3 × 3 × 3 and 5 × 5 × 5 Monkhorst–Pack *K*-points has been used for geometry optimization and density of states calculations, respectively[66]. After obtaining fully relaxed structures, the ion-migration mechanism has been examined by climbing image nudged elastic band methods for a sequence of seven images. All the structures are completely relaxed with the minimum-energy criteria until the Hellman–Feynman force decreases below 0.01 eV $Å^{-1}$.

Data availability

All data supporting this study are available within this article and its Supplementary Information. Any additional relevant data are available upon request. Source data are provided with this paper.

References

48. Parize, J. L., Medouar, A., Savariault, J. M., Ballivet-Tkatchenko, D. & Galy, J. Formation of sodium and copper vanadium oxibronzes via oxalate decomposition: thermal and X ray studies. *Mater. Res. Bull.* **24**, 1147–1153 (1989).
49. Wizansky, A. R., Rauch, P. E. & Disalvo, F. J. Powerful oxidizing agents for the oxidative deintercalation of lithium from transition-metal oxides. *J. Solid State Chem.* **81**, 203–207 (1989).
50. Sheldrick, G. M. & IUCr, A. Short history of *SHELX*. *Acta Crystallogr. A* **64**, 112–122 (2008).
51. Hübschle, C. B., Sheldrick, G. M. & Dittrich, B. *ShelXle*: a Qt graphical user interface for *SHELXL*. *J. Appl. Crystallogr.* **44**, 1281–1284 (2011).
52. Wang, W., Wang, H., Liu, S. & Huang, J. Synthesis of γ-LiV_2O_5 nanorods as a high-performance cathode for Li ion battery. *J. Solid State Electrochem.* **16**, 2555–2561 (2012).
53. Deng, Z. et al. 3D ordered macroporous MoS_2@C nanostructure for flexible Li-ion batteries. *Adv. Mater.* **29**, 1603020 (2017).
54. Lee, Y.-S. & Ryu, K.-S. Study of the lithium diffusion properties and high rate performance of $TiNb_6O_{17}$ as an anode in lithium secondary battery. *Sci. Rep.* **7**, 16617 (2017).
55. Weppner, W. & Huggins, R. A. Determination of the kinetic parameters of mixed-conducting electrodes and application to the system Li_3Sb. *J. Electrochem. Soc.* **124**, 1569–1578 (1977).
56. Piao, T., Park, S., Doh, C. & Moon, S. Intercalation of lithium ions into graphite electrodes studied by AC impedance measurements. *J. Electrochem. Soc.* **146**, 2794 (1999).

57. Wang, L. et al. Electrochemical impedance spectroscopy (EIS) study of $LiNi_{1/3}Co_{1/3}Mn_{1/3}O_2$ for Li-ion batteries. *Int. J. Electrochem. Sci.* **7**, 345–353 (2012).
58. Borkiewicz, O. J. et al. The AMPIX electrochemical cell: a versatile apparatus for in situ X-ray scattering and spectroscopic measurements. *J. Appl. Crystallogr.* **45**, 1261–1269 (2012).
59. Toby, B. H. & Von Dreele, R. B. GSAS-II: the genesis of a modern open-source all purpose crystallography software package. *J. Appl. Crystallogr.* **46**, 544–549 (2013).
60. Henkelman, G. & Jónsson, H. Improved tangent estimate in the nudged elastic band method for finding minimum energy paths and saddle points. *J. Chem. Phys.* **113**, 9978–9985 (2000).
61. Hohenberg, P. & Kohn, W. Inhomogeneous electron gas. *Phys. Rev.* **136**, B864–B871 (1964).
62. Kohn, W. & Sham, L. J. Self-consistent equations including exchange and correlation effects. *Phys. Rev.* **140**, A1133 (1965).
63. Kresse, G. & Furthmüller, J. Efficient iterative schemes for ab initio total-energy calculations using a plane-wave basis set. *Phys. Rev. B* **54**, 11169–11186 (1996).
64. Blöchl, P. E. Projector augmented-wave method. *Phys. Rev. B* **50**, 17953–17979 (1994).
65. Perdew, J. P., Burke, K. & Ernzerhof, M. Generalized gradient approximation made simple. *Phys. Rev. Lett.* **77**, 3865–3868 (1996).
66. Monkhorst, H. J. & Pack, J. D. Special points for Brillouin-zone integrations. *Phys. Rev. B* **13**, 5188–5192 (1976).

Acknowledgements

This study is based on work supported by the National Science Foundation (NSF) under DMR 1809866 (S.B.). This research used resources of the Advanced Photon Source by Argonne National Laboratory under contract number DE-AC02-06CH11357. Argonne National Laboratory is operated for the US Department of Energy Office of Science by UChicago Argonne. We thank K. Wiaderek and A. Yakovenko for their support at beamline 17-BM of the Advanced Photon Source. Use of the TAMU Materials Characterization Facility and the Texas A&M Microscopy and Imaging Center is acknowledged. M.P. acknowledges the support of National Science Foundation (NSF) under DMR 1944674. T.D. and S.C. acknowledge HRI Allahabad and DST-SERB (SRG/2020/001707) for the infrastructure and funding. Computational work for this study was carried out at the cluster computing facility at Harish-Chandra Research Institute (http://www.hri.res.in/cluster).

Author contributions

Y.L. conceptualized the project under the supervision of S.B. The powder materials were designed, synthesized and characterized and electrochemically tested by Y.L. The operando experiment was conducted by Y.L. with the help of J.V.H. The single-crystal materials were designed, synthesized and characterized by J.V.H., J.D.P. and R.A. The DFT simulations were performed by T.D. under the supervision of S.C. Galvanostatic intermittent titration technique data were acquired by Y.-H.C. Long-term electrochemical cycling was conducted by B.J.S., L.G and D.C.B. Coin cell assembly resources and advice were provided by M.P. The paper was written by Y.L. and revised by S.B., J.V.H. and J.D.P. with the help of all other authors. All authors contributed to discussions and writing—review and editing.

Competing interests

A provisional patent has been filed related to new compositions of lithiated β-$Na_{0.25}V_2O_5$/β-$K_{0.22}V_2O_5$ by the Texas A&M University System.

Additional information

Supplementary information The online version contains supplementary material available at https://doi.org/10.1038/s41563-024-01842-y.

Correspondence and requests for materials should be addressed to Sudip Chakraborty or Sarbajit Banerjee.

Peer review information *Nature Materials* thanks the anonymous reviewer(s) for their contribution to the peer review of this work.